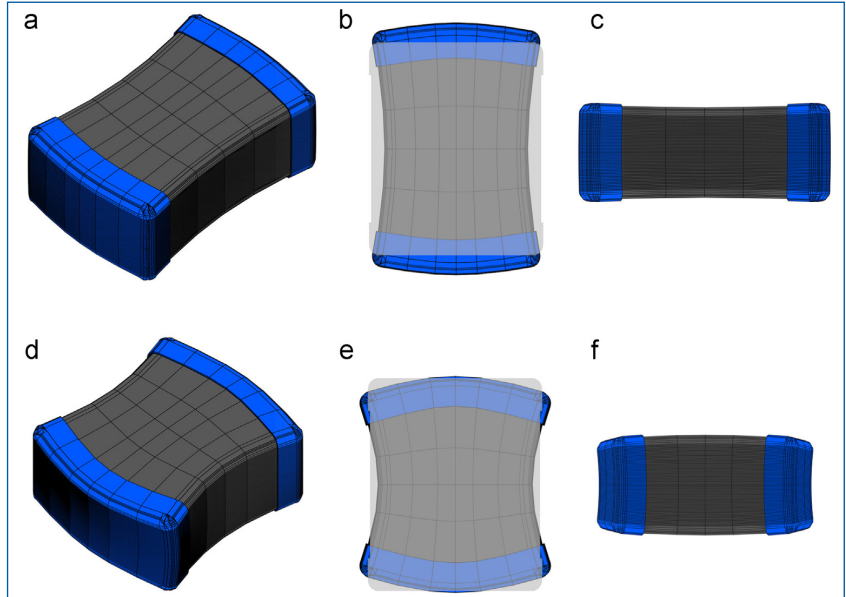


MOUNTAIN-PLAINS CONSORTIUM

MPC 18-343 | K.L. Peterson and P.R. Heyliger

MEMS Sensors for Transportation Structures



A University Transportation Center sponsored by the U.S. Department of Transportation serving the Mountain-Plains Region. Consortium members:

Colorado State University
North Dakota State University
South Dakota State University

University of Colorado Denver
University of Denver
University of Utah

Utah State University
University of Wyoming

MEMS Sensors for Transportation Structures

K. L. Peterson and P. R. Heyliger

Department of Civil and Environmental Engineering
Colorado State University
Fort Collins CO 80523
prh@engr.colostate.edu

July 2018

Disclaimer

The contents of this report reflect the views of the authors, who are reasonable for the facts and the accuracy of the information presented. This document is disseminated under the sponsorship of the Department of Transportation, University Transportation Centers Program, in the interest of information exchange. The U.S. Government assumes no liability for the contents or use thereof.

NDSU does not discriminate in its programs and activities on the basis of age, color, gender expression/identity, genetic information, marital status, national origin, participation in lawful off-campus activity, physical or mental disability, pregnancy, public assistance status, race, religion, sex, sexual orientation, spousal relationship to current employee, or veteran status, as applicable. Direct inquiries to Vice Provost, Title IX/ADA Coordinator, Old Main 201, 701-231-7708, ndsuoaaa@ndsuo.edu.

ABSTRACT

Of all microelectromechanical systems (MEMS), regardless of application, micron-scale spacing of interleaved electrodes and high-dielectric ceramics in multilayer ceramic capacitors (MLCCs) provide exceptionally high capacitances in small volumes. This has led to MLCCs being the preferred type of capacitor in a wide range of applications where size and weight are critical factors. However, crack-related failures of MLCCs remain a significant issue. Resonant ultrasound spectroscopy (RUS) and resonant nonlinear ultrasonics are being pursued as nondestructive techniques for detecting subsurface cracks that can evolve into performance-degrading electrical pathways during service. This report presents finite-element calculations of the vibrational modes of MLCCs. The geometric symmetry in the finite-element model was orthorhombic, with three orthogonal mirror planes, and the detailed internal structure of interleaved metallic and ceramic materials was included in the model. The assumption of three mirror planes enabled an analysis of the normal modes of the full model through calculations on a mesh, spanning just one eighth of the full volume. The computational load was further reduced by separating the problem into eight modal-symmetry sets with different boundary conditions for each set. The first three non-zero frequencies are presented for each modal symmetry set. In addition, displacement plots are presented for the two or three lowest-frequency modes of each symmetry set. These results provide information on the frequency ordering and symmetries of vibrational modes that can be used in the analysis of ultrasonic resonance measurements of MLCCs.

TABLE OF CONTENTS

1. INTRODUCTION.....	1
1.1 Model Device.....	2
1.1.1 Geometry.....	2
1.1.2 Materials	4
1.2 Numerical Model	4
1.2.1 Governing Equations.....	4
1.2.2 Finite Element Approximations	6
1.2.3 Symmetry Classifications and Boundary Conditions on Final Mesh.....	7
2. RESULTS	10
3. DISCUSSION	19
4. CONCLUSIONS	21
REFERENCES.....	22
APPENDIX A: COEFFICIENT MATRICES	25

LIST OF TABLES

Table 1.1	Isotropic properties as used in the analysis.....	4
Table 1.2	Reflected symmetries of the displacement components	8
Table 1.3	Effect of endcaps on first mode symmetries.....	9
Table 2.1	Calculated frequencies for each of the eight subsets	10

LIST OF FIGURES

Figure 1.1 The specimen geometry 2

Figure 2.1 OD Displacements 11

Figure 2.2 OX Displacements 12

Figure 2.3 OY Displacements 13

Figure 2.4 OZ Displacements..... 14

Figure 2.5 EX Displacements..... 15

Figure 2.6 EY Displacements..... 16

Figure 2.7 EZ Displacements 17

Figure 2.8 EV Displacements..... 18

1. INTRODUCTION

The development and commercialization of multilayer ceramic capacitors (MLCCs) has been a significant factor leading to reductions in size of a wide variety of electrical circuits, because the micron-scale spacing of interleaved electrodes and high-dielectric ceramics in MLCCs provides exceptionally high capacitance in small volumes. However, challenges exist with enhancing reliability of MLCCs associated with the intrinsic vulnerability of the dielectric ceramic material to cracking under stress during manufacture, soldering, and service [1]. Although relatively rare, crack-related failures of MLCCs remain a significant issue, especially in applications where the repercussions of failure can be catastrophic or replacement is impossible, costly or dangerous, as in implantable medical devices and spacecraft.

Established methods for screening MLCCs for flaws before and after their incorporation in electrical circuits include visual inspection and measurements of electrical leakage current [1]. However, these methods are ineffective at detecting the presence of subsurface cracks that can evolve into performance-degrading electrical pathways during service [1–3]. This situation has motivated research on acoustic inspection methods sensitive to internal structure. Such research has included work on scanning acoustic microscopy, scanning laser acoustic microscopy, resonant ultrasound spectroscopy (RUS), electromechanical resonance spectroscopy employing swept-frequency impedance analyzers, and tone-burst electromechanical resonance [2–10].

Two published studies of MLCCs have included finite-element (FE) modeling of resonant vibrational modes to support interpretation of experimental spectra [6,9]. Prume et al. [6] calculated FE impedance spectra with piezoelectric and dielectric terms included in the equation of motion and the excitation provided through direct ferroelectric coupling to electric fields applied to the internal interleaved electrodes. The transduction mechanism in this model and corresponding impedance measurements introduces restrictions on the excited modal symmetries. Capacitors with industrial size designations of 1210 and 1812 were included in these models, and the effects of delaminations and idealized cracks with two different orientations were explored through comparisons of calculated and experimental spectra. Johnson et al. [9] reported FE normal-mode spectra and displacement patterns for several resonant modes near the dominant experimentally measured resonant peaks of smaller type-0603 MLCCs driven with ferroelectric excitation. The FE model in that study did not include ferroelectric excitation or piezoelectric/ dielectric terms in the equation of motion.

The current report presents FE calculations of acoustic normal modes of all symmetry types, based on an MLCC model with dimensions and internal structure approximately matching those previously reported for a set of type-1210 MLCCs [10]. Internal interleaved layers of electrodes and ceramic are explicitly included in the model, although the geometry of these layers is approximated as orthorhombic to reduce the size of the computational problem (as in the work of Prume et al. [6]). Piezoelectric and dielectric terms are not included in the equation of motion. The inclusion of all modal symmetries in the model is anticipated to facilitate interpretation of RUS measurements, which are not limited to excitation of specific symmetries. The research reported here is specifically associated with experimental work that has been reported elsewhere on the detection of cracks in MLCCs through RUS [8] and tone-burst electromechanical resonance [10].

1.1 Model Device

1.1.1 Geometry

The geometry in the FE model considered here is shown in Figure 1.1 and is based on measurements reported by Johnson et al. [10] for a set of type-1210 MLCCs manufactured by Vishay Inter-technology with model number of VJ1210Y474KXAAT.¹

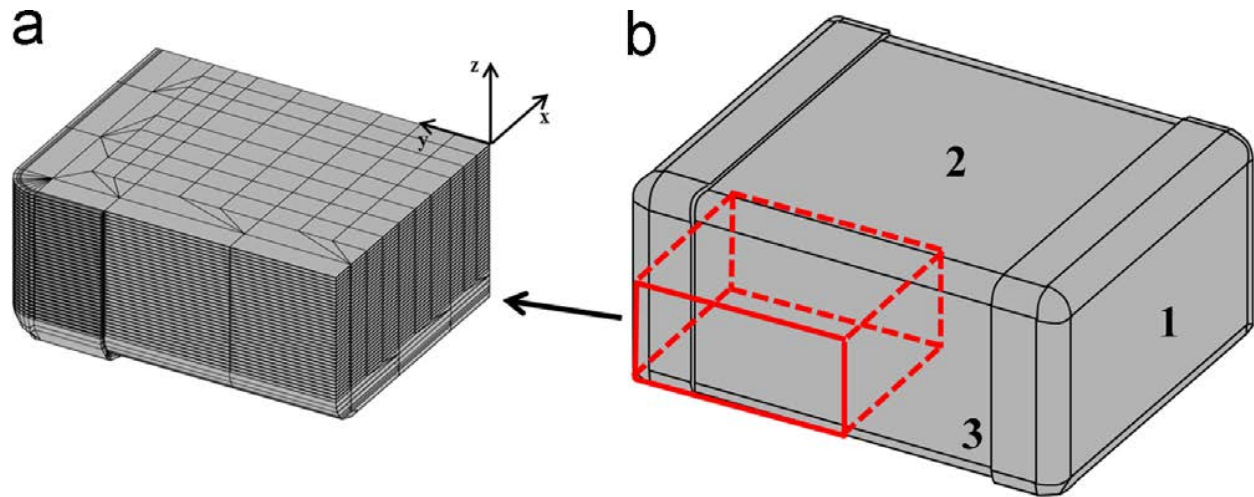


Figure 1.1 The specimen geometry. (a) Magnified view of the single octant that is meshed and analyzed in the finite-element calculation and (b) geometry of the entire capacitor. The metal endcaps of the capacitor appear as raised areas with rounded edges. The darker grey regions in (a) represent the finely interleaved layers of ceramic and metallic electrodes with their largest surfaces in the x - y plane. Surface labels are defined in (b) as 1, 2, and 3.

The three exterior surfaces of the capacitor shown in Figure 1.1 (b) are defined for the purpose of describing the displacement pattern results. The endcap surface (with surface-normal vector in the \hat{y} direction) is Surface 1, the larger capacitor surface (with surface-normal vector in the \hat{z} direction) is Surface 2, and the smaller capacitor surface (with surface-normal vector in the \hat{x} direction) is Surface 3. As described by Johnson et al. [10], the 70 electrodes in the core of the physical MLCC have a thickness of $2.0\ \mu\text{m}$ and a periodicity of $16.38\ \mu\text{m}$, corresponding to a total thickness of $1.132\ \text{mm}$ for the interleaved core region. The width and length of the internal electrodes are $2.068\ \text{mm}$ and $2.852\ \text{mm}$, respectively, and connect alternately to the two metallic endcaps of the MLCC. The electrodes are surrounded by a ceramic filler material (a typical dielectric for MLCCs described in a subsequent section) with overall dimensions of $2.474\ \text{mm}$, $3.040\ \text{mm}$, and $1.414\ \text{mm}$. The endcaps each consist of three metallic layers. The thicknesses of the metallic layers from outside to inside (tin, nickel, and silver, respectively) are $15.0\ \mu\text{m}$, $9.0\ \mu\text{m}$, and $7.0\ \mu\text{m}$, for a total thickness on one end of $31.0\ \mu\text{m}$, resulting in final overall dimensions of $2.536\ \text{mm}$, $3.102\ \text{mm}$, and $1.476\ \text{mm}$ in the \hat{x} , \hat{y} , and \hat{z} directions, respectively, shown in Figure 1.1.

Nominal symmetry of the physical MLCCs is monoclinic (corresponding to the group-theoretical point group C_{2h} in the Schoenflies notation), with one mirror plane ($y-z$) and a two-fold rotation axis (\hat{x}) normal to this plane [11]. The exterior surfaces of the physical MLCC, as depicted in Figure 1.1(b), have a higher symmetry corresponding to the orthorhombic point group D_{2h} , with three mirror planes and corresponding two-fold rotation axes and inversion symmetry [11]. The reduced symmetry of the full capacitor arises from the fact that alternating connections of the even number of internal electrodes to the endcaps eliminates two of the mirror planes. In this study, reduction in symmetry of the physical MLCC is neglected, and total symmetry of the capacitor is approximated as D_{2h} . This approximation of higher symmetry is implemented in the model by having the electrodes in the model alternately connect to either both endcaps or neither endcap, rather than and alternately to one or the other endcap as in the physical capacitor. This is equivalent to shifting the location of a portion of the internal electrode material near the endcaps by one period (16.38 μm) of the interleaved structure. The effect of this approximation is expected to be insignificant because (1) it shifts the position of electrode material by only a small fraction of the exterior dimensions, (2) it does not change the relative volumes of the materials in the capacitor and (3) it does not lead to an introduction or splitting of degenerate modes, because there are no degeneracies in either the C_{2h} or the D_{2h} point groups. Also, the thicknesses of the ceramic material above and below the core region of the physical MLCCs can vary from capacitor to capacitor. For simplicity, it was assumed for the mesh that the $x-y$ midplane falls exactly between two layers. Therefore, because the mesh assumes symmetry across the $x-y$ reflection plane, an electrode with double the thickness appears at the very center of the mesh, and this feature does not exist in the physical MLCC. Again, because this assumption does not change the volume fraction of the materials, it is a useful approximation that significantly reduces the size of the computational problem.

The D_{2h} symmetry of the model enables the FE calculations to be performed on only one octant of the MLCC (as shown in Figure 1.1), with boundary conditions specified to match the specified modal symmetries. This resulted in a mesh with 75 total layers of elements in the \hat{z} direction within the octant. The curved bottom ceramic region was modeled with five layers of elements through the thickness. Each pair of electrode and ceramic layers (every 16.38 μm) was modeled with two elements through the thickness, resulting in 70 total layers of elements for the core region, 35 including dielectric and electrode materials and 35 with only dielectric material. As described below, the endcaps have a relatively small effect on the frequencies. Therefore, highly exact modeling of the endcaps is assumed not to be critical, and, to save on computational time, the endcaps were modeled with only one element through the thickness of each metallic endcap layer. The capacitor octant mesh has overall dimensions of 1.268 mm, 1.551 mm, and 0.738 mm in the \hat{x} , \hat{y} , and \hat{z} directions, respectively. These values are half of the overall dimensions given for the whole capacitor. A generally square mesh was implemented for the layers, and corners were modeled with triangular wedge elements extending radially. This mesh geometry is shown in Figure 1.1. A convergence study to determine the appropriate refinement of this core region of the mesh is described in a subsequent section. Triangular wedge elements were also used to connect the coarser portion of the mesh for the curved bottom ceramic region with the refined core region. The origin of the coordinate system is located at the center of the full capacitor. The total volume of the meshed octant (one eighth of entire capacitor) is $1.369 \times 10^{-9} \text{ m}^3$.

1.1.2 Materials

The interior electrodes and interior layer of the endcaps are composed of silver (Ag), the second layer of the endcaps is a thin nickel (Ni) diffusion barrier, and the outer layer of the endcaps is tin (Sn). Doped polycrystalline barium titanate (BaTiO_3), a typical dielectric for MLCCs, fills spaces between the electrodes and the regions without electrodes near the surfaces of the capacitor.

Dopant levels and corresponding elastic-stiffness of BaTiO_3 used in MLCCs are dependent on the capacitor manufacturer [12]. Accurate ultrasonic measurements of elastic stiffness of individual MLCCs are challenging, given the small volumes of ceramic regions without interleaved electrodes. Values of elastic stiffness of pure BaTiO_3 employed here for finite element calculations were derived through the use of the method of Kim [13] from sets of published room-temperature measurements of diagonal elements of elastic stiffness and compliance tensors. This approach avoids typically substantial uncertainties in reported off-diagonal elements of the tensors. Uncertainties in off-diagonal elements arise from the fact that these elements are not simply related to measurements of any pure mode of mechanical deformation [14,15]. Diagonal elements of the elastic stiffness tensor of pure BaTiO_3 published by Zgonik et al. [16] and diagonal elements of the elastic compliance tensor published by Berlincourt and Jaffe [17] were used here to determine the single-crystal elastic stiffness constants C_{11} , C_{33} , C_{12} , and C_{13} of BaTiO_3 through the use of the method of Kim [13]. These elements of the stiffness tensor were then employed to estimate isotropic polycrystalline values through an arithmetic Voigt–Reuss–Hill average [18]. The resultant material properties for the BaTiO_3 -based ceramic are shear modulus of 56.6 GPa, bulk modulus of 141.5 GPa, Young's modulus of 149.8 GPa, and Poisson ratio of 0.3235. These values were used to calculate the elastic stiffness constants listed in Table 1.1. The value for the density of BaTiO_3 is that given by Urek and Drogenik [19]. Table 1.1 also lists the C_{11} and C_{44} values for Ag [20], Ni [21], and Sn. The values of the elastic constants for Sn are a simple average of values listed by Simmons and Wang [22] for their calculations of Voigt–Reuss aggregate averages using single-crystal constants that were measured by Rayne and Chandrasekhar [23].

Table 1.1 Isotropic properties as used in the analysis

Material	C_{11} (GPa)	C_{44} (GPa)	Density (kg/m ³)
BaTiO_3	217.0	56.6	6050
Sn	78.8	17.9	7297
Ag	141.5	30.2	10,501
Ni	298.9	84.7	8909

1.2 Numerical Model

1.2.1 Governing Equations

In this section, the weak form of the equations of motion of a homogeneous orthorhombic solid are derived to provide the basis for finite-element modeling [24], and the approximate displacements and numerical method are discussed. The equations are presented in terms of

rectangular Cartesian coordinates, which enable the eigenvalue problem to be separated according to geometric and material symmetries. This drastically reduces the computational load involved in the finite-element calculations [25]. The three independent displacement components are expressed as $u = u(x, y, z)$, $v = v(x, y, z)$, and $w = w(x, y, z)$, and correspond to displacements in the \hat{x} , \hat{y} , and \hat{z} directions, respectively. The general constitutive relation for the material can be expressed as

$$\begin{Bmatrix} \sigma_1 \\ \sigma_2 \\ \sigma_3 \\ \sigma_4 \\ \sigma_5 \\ \sigma_6 \end{Bmatrix} = \begin{bmatrix} C_{11} & C_{12} & C_{13} & 0 & 0 & 0 \\ C_{12} & C_{22} & C_{23} & 0 & 0 & 0 \\ C_{13} & C_{23} & C_{33} & 0 & 0 & 0 \\ 0 & 0 & 0 & C_{44} & 0 & 0 \\ 0 & 0 & 0 & 0 & C_{55} & 0 \\ 0 & 0 & 0 & 0 & 0 & C_{66} \end{bmatrix} \begin{Bmatrix} \epsilon_1 \\ \epsilon_2 \\ \epsilon_3 \\ \epsilon_4 \\ \epsilon_5 \\ \epsilon_6 \end{Bmatrix}$$

Here, σ_i represents the components of stress in contracted notation, C_{ij} the components of the elastic stiffness tensor computed from the elastic properties listed in Table 1.1 and represented in standard matrix form [26], and ϵ_i the components of strain in contracted notation.

Correspondence of the contracted notation and standard indicial notation for a second-order tensor is given, for the specific stress, elastic stiffness, and strain components, by $\sigma_1 = \sigma_{11}$, $\sigma_2 = \sigma_{22}$, $\sigma_3 = \sigma_{33}$, $\sigma_4 = \sigma_{23}$, $\sigma_5 = \sigma_{13}$, $\sigma_6 = \sigma_{12}$, $C_{11} = C_{1111}$, $C_{12} = C_{1122}$, $C_{13} = C_{1133}$, $C_{22} = C_{2222}$, $C_{23} = C_{2233}$, $C_{33} = C_{3333}$, $C_{44} = C_{2323}$, $C_{55} = C_{1313}$, $C_{66} = C_{1212}$, $\epsilon_1 = \epsilon_{11}$, $\epsilon_2 = \epsilon_{22}$, $\epsilon_3 = \epsilon_{33}$, $\epsilon_4 = 2\epsilon_{23} = \gamma_{23}$, $\epsilon_5 = 2\epsilon_{13} = \gamma_{13}$, and $\epsilon_6 = 2\epsilon_{12} = \gamma_{12}$ [27]. The representative directions defined by the subscripts will be identified for each case below.

The relationships between strain and displacement are

$$\begin{aligned} \epsilon_1 &= \frac{\partial u}{\partial x} & \epsilon_2 &= \frac{\partial v}{\partial y} \\ \epsilon_3 &= \frac{\partial w}{\partial z} & \epsilon_4 &= \frac{\partial v}{\partial z} + \frac{\partial w}{\partial y} \\ \epsilon_5 &= \frac{\partial u}{\partial z} + \frac{\partial w}{\partial x} & \epsilon_6 &= \frac{\partial v}{\partial x} + \frac{\partial u}{\partial y} \end{aligned}$$

Hamilton's principle provides the starting point for each of the subsequent derivations. This can be written in the absence of a body force and surface traction as

$$\begin{aligned} 0 &= - \int_0^t \int_v \{ \sigma_1 \delta \epsilon_1 + \sigma_2 \delta \epsilon_2 + \sigma_3 \delta \epsilon_3 + \sigma_4 \delta \epsilon_4 + \sigma_5 \delta \epsilon_5 + \sigma_6 \delta \epsilon_6 \} dV dt \\ &\quad + \frac{1}{2} \delta \int_0^t \int_v \rho (\dot{u}^2 + \dot{v}^2 + \dot{w}^2) dV dt \end{aligned}$$

where V is the volume of the solid, $\dot{u} = \frac{\partial u}{\partial t}$, t is time, ρ is mass density, and δ is the variational operator. Substitution of Eqs. (1) and (2) into Eq. (3), and with the assumption of harmonic motion for each of the displacement components gives the specific weak form of Hamilton's principle:

$$\begin{aligned}
0 = \int_V & \left[\left(C_{11} \frac{\partial u}{\partial x} + C_{12} \frac{\partial v}{\partial y} + C_{13} \frac{\partial w}{\partial z} \right) \frac{\partial \delta u}{\partial x} + \left(C_{12} \frac{\partial u}{\partial x} + C_{22} \frac{\partial v}{\partial y} + C_{23} \frac{\partial w}{\partial z} \right) \frac{\partial \delta v}{\partial y} \right. \\
& + \left(C_{13} \frac{\partial u}{\partial x} + C_{23} \frac{\partial v}{\partial y} + C_{33} \frac{\partial w}{\partial z} \right) \frac{\partial \delta w}{\partial z} + C_{44} \left(\frac{\partial v}{\partial z} + \frac{\partial w}{\partial y} \right) \left(\frac{\partial \delta v}{\partial z} + \frac{\partial \delta w}{\partial y} \right) \\
& + C_{55} \left(\frac{\partial u}{\partial z} + \frac{\partial w}{\partial x} \right) \left(\frac{\partial \delta u}{\partial z} + \frac{\partial \delta w}{\partial x} \right) + C_{66} \left(\frac{\partial u}{\partial y} + \frac{\partial v}{\partial x} \right) \left(\frac{\partial \delta u}{\partial y} + \frac{\partial \delta v}{\partial x} \right) \\
& \left. - \rho \omega^2 (u \delta u + v \delta v + w \delta w) \right] dV.
\end{aligned}$$

If necessary, these equations can be integrated by parts to give the differential equations of motion for the solid. They are not listed here.

1.2.2 Finite Element Approximations

Approximate solutions to the weak form of the equations of motion given in the previous section can be generated using piecewise approximations of the three displacement components over small domains. This is accomplished by approximating the displacement components u , v , and w using finite linear combinations of the form:

$$u(x, y, z) = \sum_{j=1}^n u_j \phi_j^u(x, y, z) \quad \delta u = \phi_i^u(x, y, z)$$

$$v(x, y, z) = \sum_{j=1}^n v_j \phi_j^v(x, y, z) \quad \delta v = \phi_i^v(x, y, z)$$

$$w(x, y, z) = \sum_{j=1}^n w_j \phi_j^w(x, y, z) \quad \delta w = \phi_i^w(x, y, z)$$

Here, ϕ_j^u , ϕ_j^v , and ϕ_j^w are known functions of position that are taken as the independent shape functions associated with a conventional 8-noded brick finite element [28], n is the number of terms in the approximation for the displacement components and the number of nodes per element, and u_j , v_j , and w_j are the nodal values of successive displacements at fixed geometric locations of the finite-element domain. In this study, they are located at the corners of each individual element [24].

For the problem of free vibration, the boundary conditions are the natural type because all faces of the solid are stress free. In the finite element method, the natural boundary conditions are contained in the variational statement of the problem. Hence, there is no need to explicitly satisfy these conditions. Because of the layered nature of the capacitor, the usual conditions of displacement and traction continuity across a dissimilar material interface are satisfied, but in varying degrees. Specifically, the enforcement of displacement continuity across the interface is explicitly satisfied only at the nodal locations of the contiguous finite elements.

In this study, the same form of approximation functions is used for each of the displacements. Given the geometric and material symmetry of the solids considered, approximation functions can be grouped in such a manner that smaller eigenvalue problems can be uncoupled from one another and solved separately. By grouping the approximation functions into odd and even reflection classifications, the total problem can be uncoupled into eight smaller problems where the matrix is of order 81. The classifications employed here for orthorhombic symmetry will be described in detail in a subsequent section and are discussed by Ohno [29].

Substitution of the approximate displacements and their variations into the weak forms and collection of terms allows for writing the equation to be solved in matrix form as:

$$\begin{bmatrix} [K^{11}] & [K^{12}] & [K^{13}] \\ [K^{21}] & [K^{22}] & [K^{23}] \\ [K^{31}] & [K^{32}] & [K^{33}] \end{bmatrix} \begin{Bmatrix} \{a\} \\ \{b\} \\ \{d\} \end{Bmatrix} - \rho\omega^2 \begin{bmatrix} [M^{11}] & 0 & 0 \\ 0 & [M^{22}] & 0 \\ 0 & 0 & [M^{33}] \end{bmatrix} \begin{Bmatrix} \{a\} \\ \{b\} \\ \{d\} \end{Bmatrix} = \begin{Bmatrix} \{0\} \\ \{0\} \\ \{0\} \end{Bmatrix},$$

where the explicit forms of the coefficient matrices are given in the Appendix. The required integration for each element is accomplished using Gauss quadrature [24]. The resulting eigenvalue problem is solved by the use of the QR algorithm [30] to provide the frequencies and eigenvectors containing the representation of displacement patterns of vibration.

1.2.3 Symmetry Classifications and Boundary Conditions on Final Mesh

As discussed in the previous section, for the problem of free vibration of a solid, the boundary conditions are all the natural type, and the natural boundary conditions are contained in the variational statement of the problem. Therefore, if the full capacitor were meshed, there would be no need to explicitly satisfy these conditions. However, because the mesh uses symmetry across three reflection planes and only one-eighth of the MLCC is modeled, the analysis was completed using eight different boundary condition sets corresponding to the eight symmetry classifications. For the eight classifications, the displacements (u , v , and w) are either even (E) or odd (O) with respect to the three reflection planes [29], as summarized in Table 1.2. The ‘‘Subset’’ column of Table 1.2 lists the symmetry classifications in both Ohno's [29] notation and a common form of group-theoretical notation [31]. In group theory, these symmetry classifications correspond to the irreducible representations of the D_{2h} point group, which is the orthorhombic point group with the most symmetry elements. For the remainder of this report, Ohno's notation will be used. The last three columns of Table 1.2 list the symmetries of the displacement components with respect to the reflection planes with surface-normal vectors of \hat{x} , \hat{y} , and \hat{z} .

Different nodal degrees of freedom (DOF) were specified to zero for the boundary conditions of the eight subsets described in Table 1.2. The DOFs set to zero correspond to the displacements that are odd (O) with respect to reflection across the corresponding reflection planes. For example, the OD type has three sets of DOFs set to zero: u displacement of all nodes on the symmetry plane with the normal vector in the \hat{x} direction, v displacement of all nodes on the symmetry plane with the normal vector in the \hat{y} direction, and w displacement of all nodes on the symmetry plane with the normal vector in the \hat{z} direction. Similarly, the EX type has the following DOFs set to zero: v and w displacements of all nodes on the symmetry plane with the normal vector in the \hat{x} direction, v displacement of all nodes on the symmetry plane with the normal vector in the \hat{y} direction, and w displacement of all nodes on the symmetry plane with the normal vector in the \hat{z} direction. A similar pattern follows for all “O” shown in Table 1.2.

Table 1.2 Reflection symmetries of the displacement components

Subset	Component	x	y	z
OD (A1g)	u	O	E	E
	v	E	O	E
	w	E	E	O
EX (B3u)	u	E	E	E
	v	O	O	E
	w	O	E	O
EY (B2u)	u	O	O	E
	v	E	E	E
	w	E	O	O
EZ (B1u)	u	O	E	O
	v	E	O	O
	w	E	E	E
OX (B3g)	u	O	O	O
	v	E	E	O
	w	E	O	E
OY (B2g)	u	E	E	O
	v	O	O	O
	w	O	E	E
OZ (B1g)	u	E	O	E
	v	O	E	E
	w	O	O	O
EV (A1u)	u	E	O	O
	v	O	E	O
	w	O	O	E

Several meshes were tested to study the effect of the endcaps and to perform a convergence study on refinement of the mesh through the core region of electrodes. Studying the effect of the endcaps was important, because removing the endcaps from the mesh reduced the computational time required to analyze the capacitor and a convergence study could be performed more efficiently. It is also of interest to explore the effect of variations in the geometry of endcaps because visible variations in this geometry exist in physical capacitors. The effect that the endcaps had on the first mode frequencies of each subset is shown in Table 1.3. On average, the absence of the endcaps increased the first frequency of each symmetry classification by 3.4%. Therefore, the endcaps decrease the frequencies, which is expected with the addition of material.

With the endcaps removed (3.77% volume decrease), a convergence study was performed on the mesh refinement of the layers. The first mesh tested consisted of 1748 elements and 2387 nodes, corresponding to a total of 7161 degrees of freedom. The number of elements per layer of the mesh was increased incrementally until less than a 1% change in frequencies was observed. The final mesh of the layers has over four times the number of degrees of freedom in comparison to the first mesh. After completion of the convergence study, the endcaps were added back to the model. The final mesh with endcaps, which was employed to obtain the frequency and mode shape results presented in the remainder of this report, consists of 9,550 elements and 10,435 nodes, corresponding to a total of 31,305 degrees of freedom. The reflection planes with \hat{x} , \hat{y} , and \hat{z} surface normals have 1039, 811, and 142 nodes, respectively.

Table 1.3 Effect of endcaps on first mode frequencies

Type	Frequency with Endcaps (MHz)	Frequency without Endcaps (MHz)
OD	0.7088	0.7299
EX	0.5899	0.6158
EY	0.8028	0.8272
EZ	0.4742	0.4907
OX	0.7720	0.7920
OY	0.7011	0.7239
OZ	0.6569	0.6701
EV	0.3543	0.3732

2. RESULTS

Analyses were completed for each subset with the corresponding boundary conditions. There were six total zero frequencies (one per subset) present in the results of the following subsets, corresponding to the six rigid-body modes: EX (translation in \hat{x}), EY (translation in \hat{y}), EZ (translation in \hat{z}), OX (rotation about \hat{x}), OY (rotation about \hat{y}), and OZ (rotation about \hat{z}). The first two non-zero frequencies (eigenvalues from the FE analysis) and their corresponding mode shapes for all subsets are presented here. The displacement values of each node are given in the eigenvectors from the FE analysis output, and the mode shapes were plotted with updated nodal locations calculated by adding (or subtracting) these displacements to the original nodal locations. The third frequency for each subset is also given. Displacement patterns for the third modes are not presented here, with the exception of the mode with OD symmetry. This OD mode is especially relevant to the interpretation of some types of experimental results, because it is the dominant mode excited through direct ferroelectric transduction [10].

Even though displacements were only calculated for an eighth of the capacitor, the mode shapes were reflected across the symmetry planes (based on the symmetry patterns shown in Table 2.1), enabling the displacement pattern for the entire capacitor to be plotted for all the mode shapes. Frequency values are listed in Table 2.1 and corresponding modal displacement patterns are plotted in Figures 2.1–2.8. Multiple orientations are shown in the displacement plots to more clearly show the symmetries.

Table 2.1 Calculated frequencies for each of the eight subsets

Subset	First frequency (MHz)	Second frequency (MHz)	Third frequency (MHz)
EV	0.3543	0.8621	1.1356
EZ	0.4742	0.6914	1.1045
EX	0.5899	1.0342	1.4184
OZ	0.6569	1.2062	1.4067
OY	0.7011	0.9699	1.0825
OD	0.7088	0.8484	0.9769
OX	0.7720	0.8762	1.2340
EY	0.8028	1.0775	1.3549

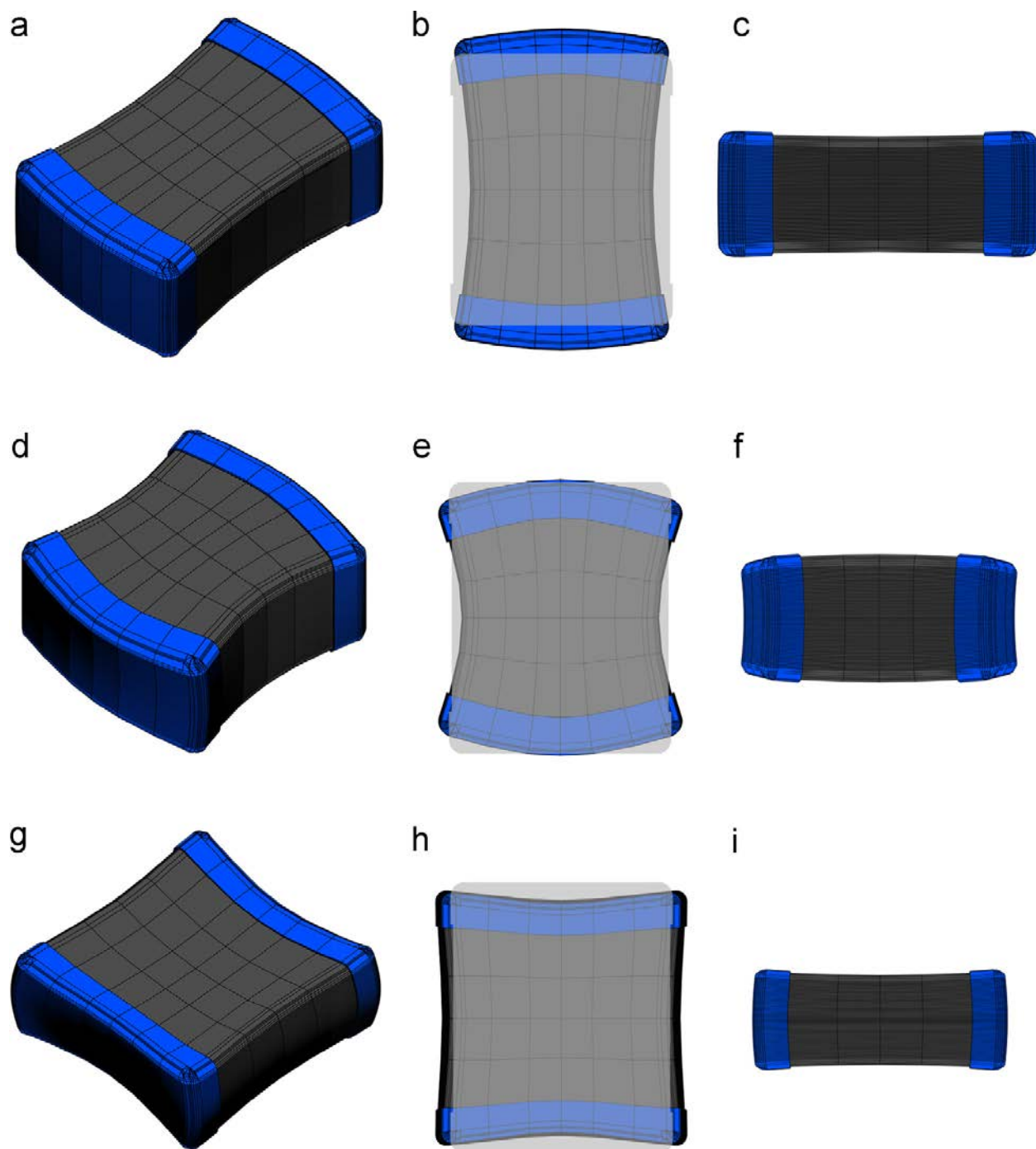


Figure 2.1 OD (A1g) displacements: (a) 0.7088 MHz—first mode isometric view, (b) first mode top view, (c) first mode side view, (d) 0.8484 MHz—second mode isometric view, (e) second mode top view, (f) second mode side view, (g) 0.9769 MHz – third mode isometric view, (h) third mode top view, and (i) third mode side view. The undistorted capacitor is shown in (b), (e), and (h) for clarification when the results are discussed.

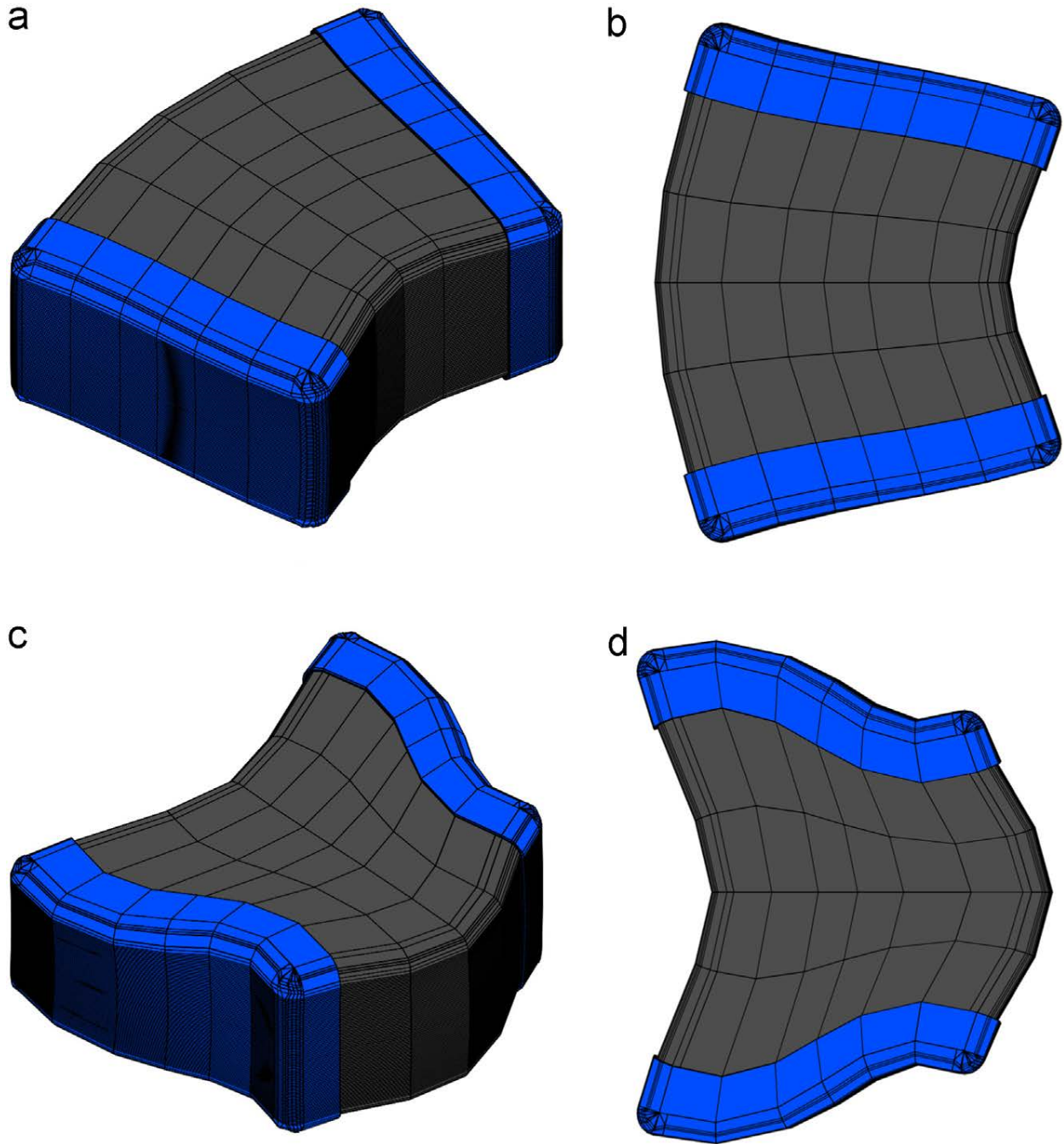


Figure 2.2 EX (B) displacements: (a) 0.5899 MHz—first mode isometric view, (b) first mode top view, (c) 1.0342 MHz—second mode isometric view, and (d) second mode top view.

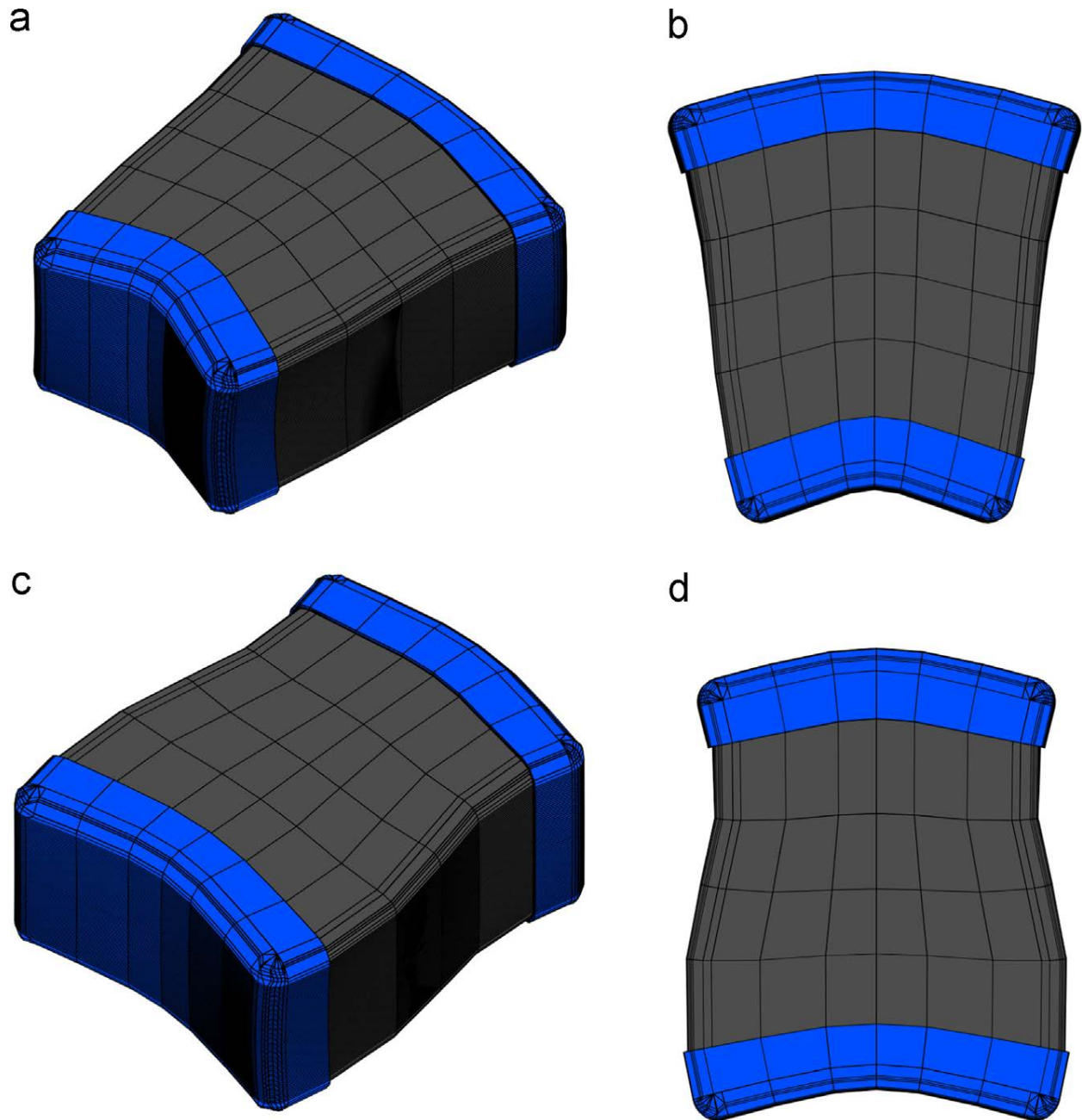


Figure 2.3 EY ($B2u$) displacement patterns: (a) 0.8028 MHz—first mode isometric view, (b) first mode top view, (c) 1.0775 MHz—second mode isometric view, and (d) second mode top view.

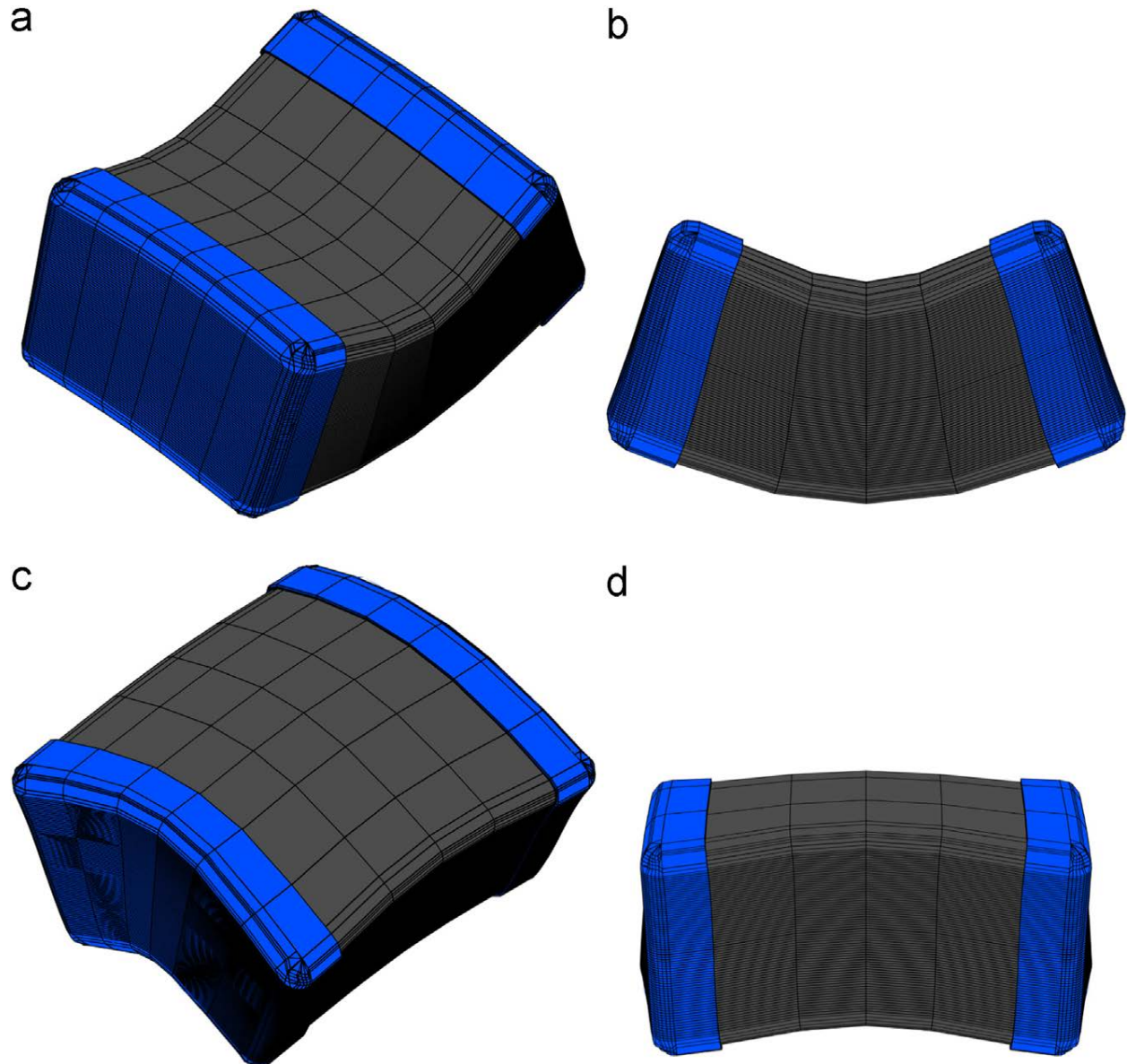


Figure 2.4 EZ (B1*u*) displacement patterns: (a) 0.4742 MHz—first mode isometric view, (b) first mode side view, (c) 0.6914 MHz—second mode isometric view, and (d) second mode side view.

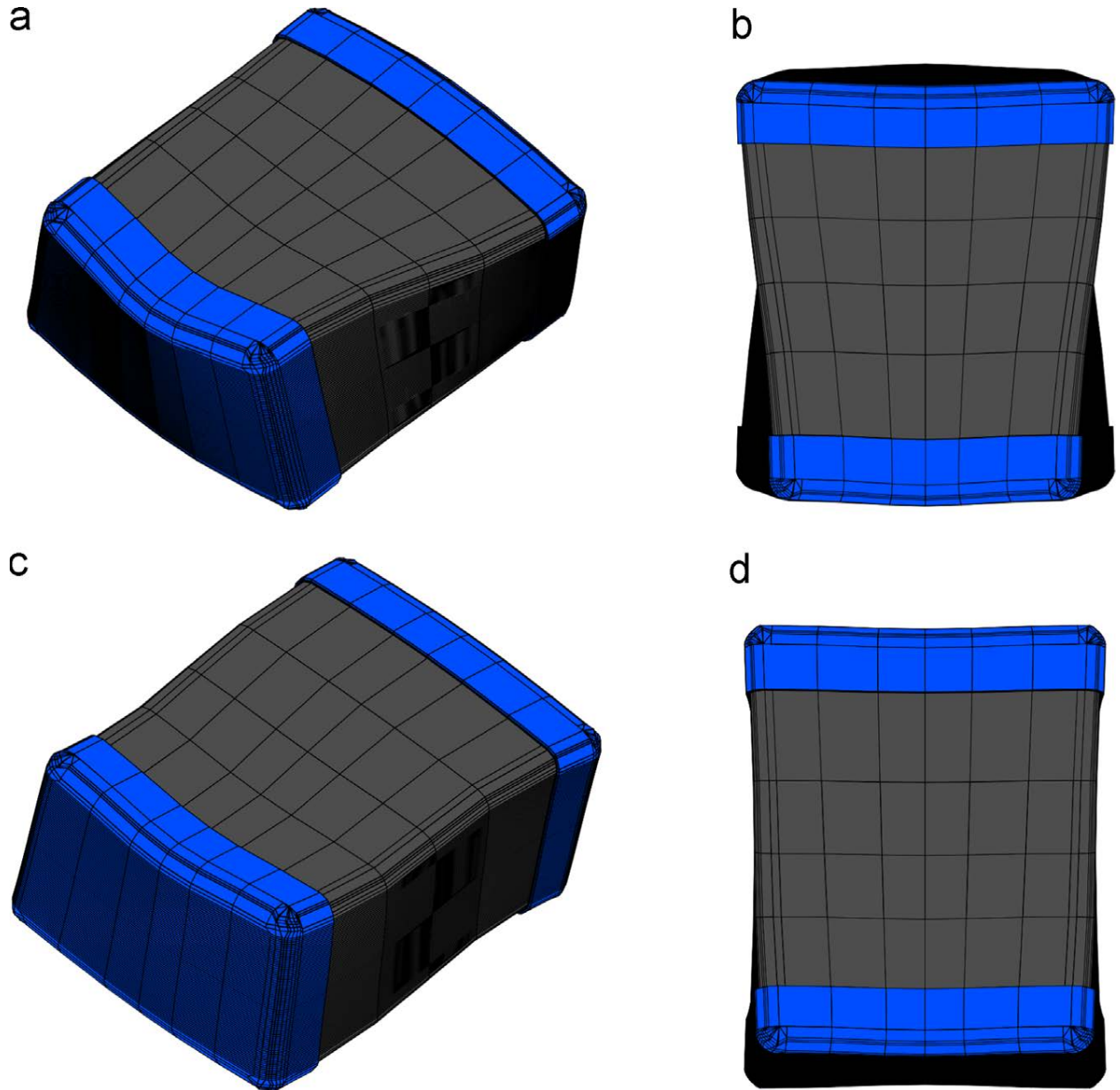


Figure 2.5 OX (B3g) displacement patterns: (a) 0.7720 MHz—first mode isometric view, (b) first mode top view, (c) 0.8762 MHz—second mode isometric view, and (d) second mode top view.

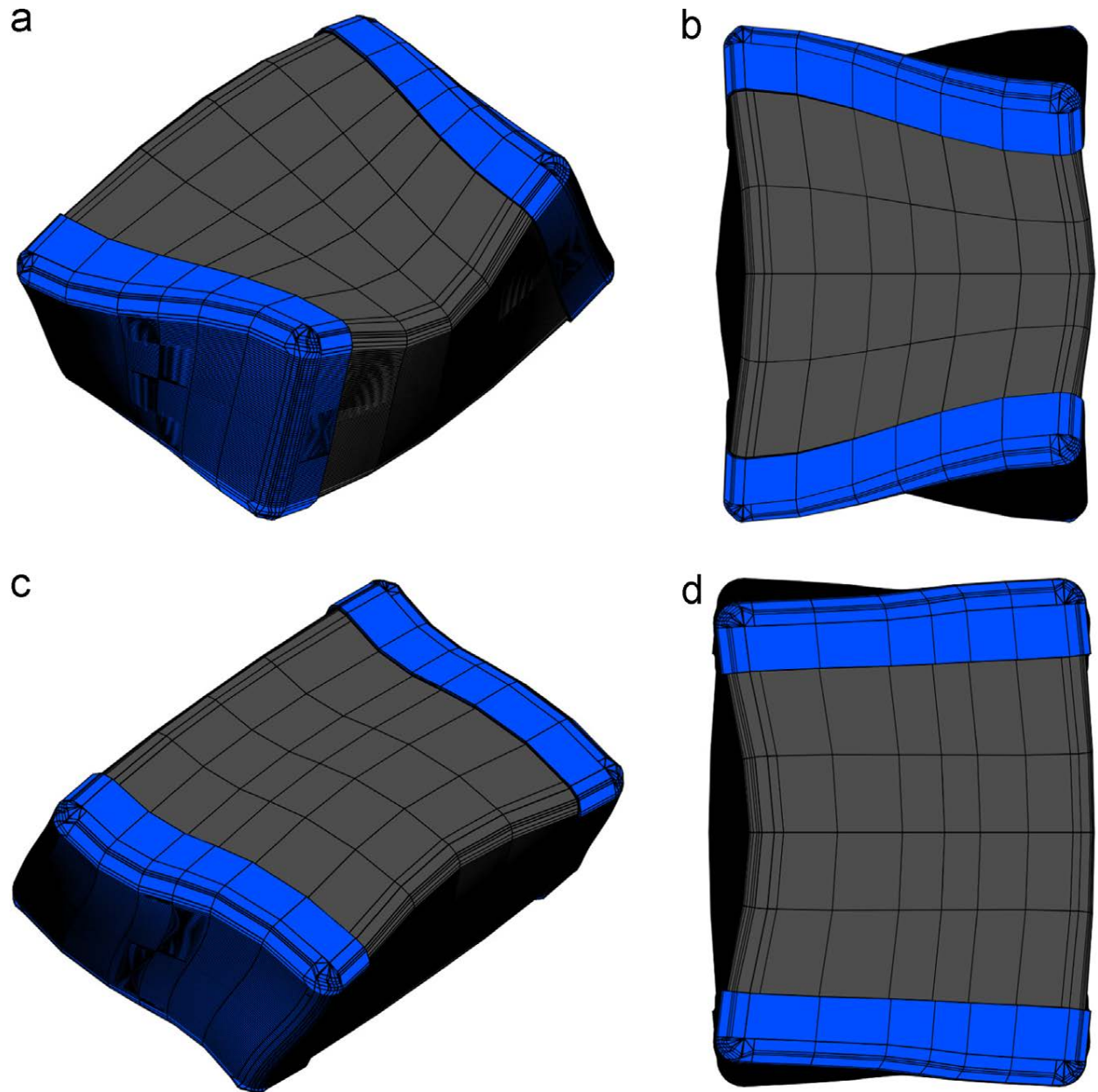


Figure 2.6 OY (B2g) displacement patterns: (a) 0.7011 MHz—first mode isometric view, (b) first mode top view, (c) 0.9699 MHz—second mode isometric view, and (d) second mode top view.

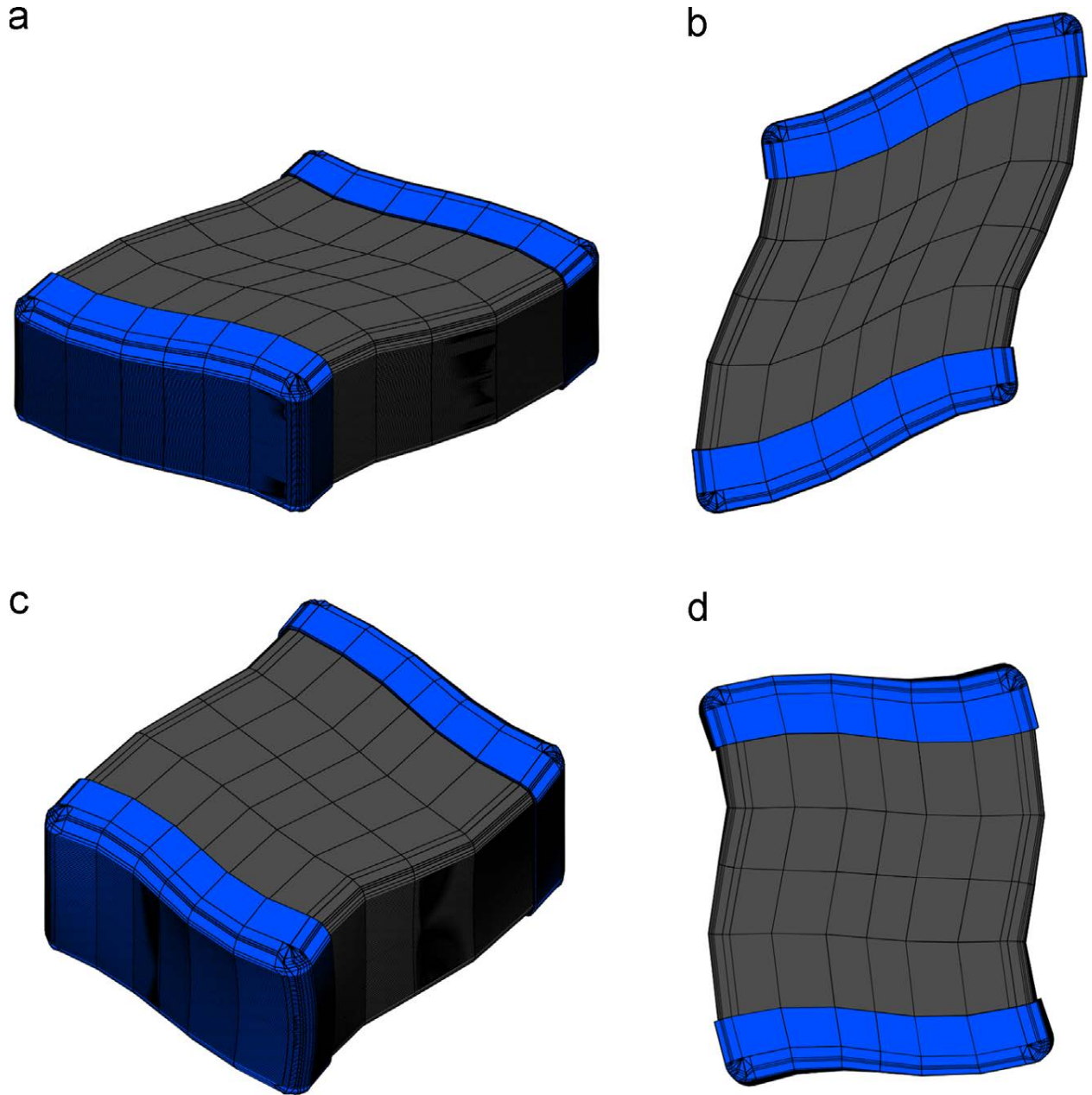


Figure 2.7 OZ (B1g) displacement patterns: (a) 0.6569 MHz—first mode isometric view, (b) first mode top view, (c) 1.2062 MHz—second mode isometric view, and (d) second mode top view.

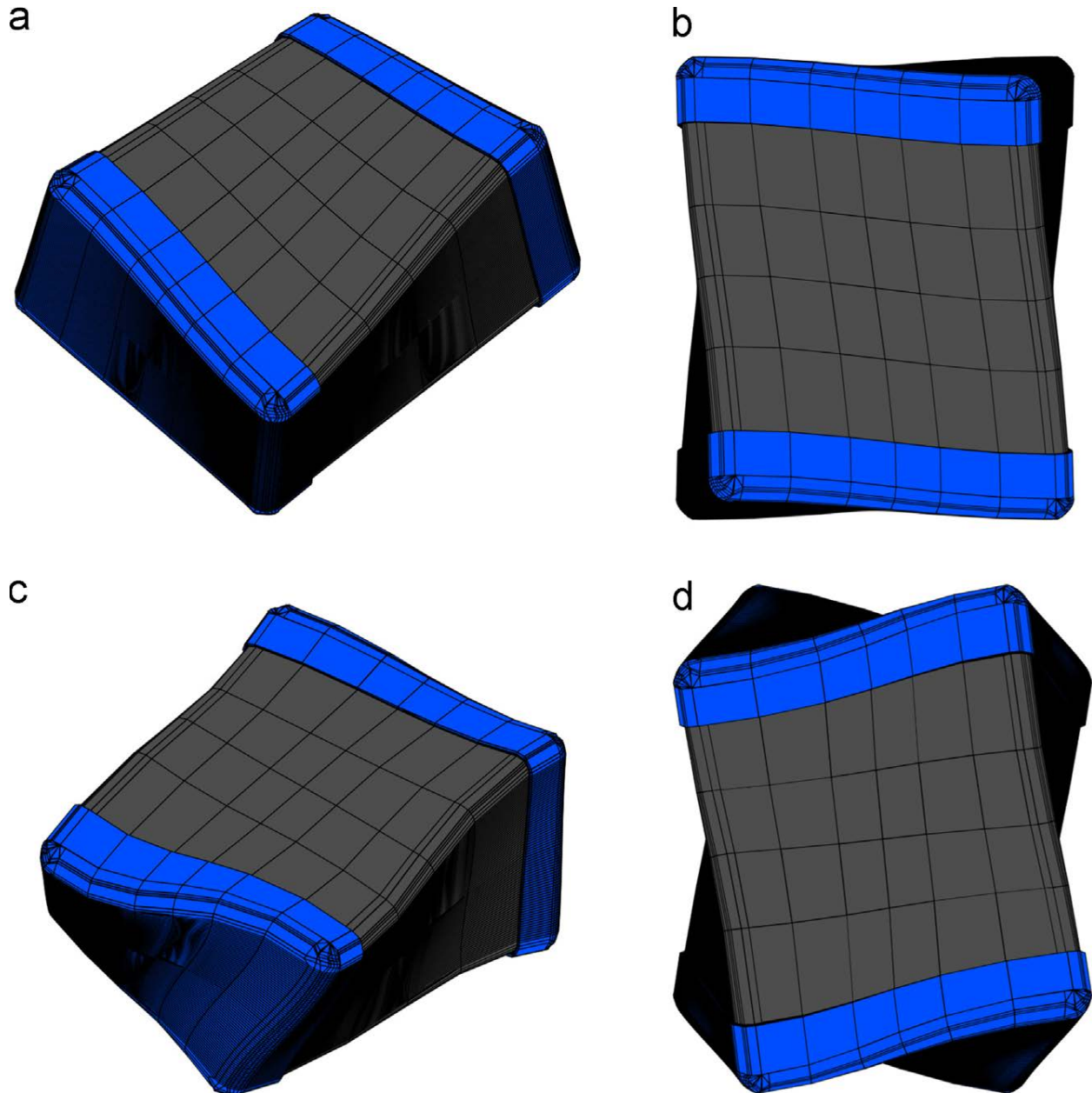


Figure 2.8 EV ($A1u$) displacement patterns: (a) 0.3543 MHz—first mode isometric view, (b) first mode top view, (c) 0.8621 MHz—second mode isometric view, and (d) second mode top view.

3. DISCUSSION

For modes whose deformation can be considered as primarily bending or flexure, most cross-sections have a weak-bending axis and a strong-bending axis. Bending modes are typically characterized by displacements on the bounding surfaces of the capacitor that act in a direction that is normal to the surface and are symmetric about one of the two bisecting axes of the surface and asymmetric about the other. For example, referring to Figure 1.1 (b), two possible bending modes correspond to bending of Surface 2 about either the x -axis or the y -axis. The former case is actually the lowest flexural mode and occurs in the EZ subset (0.4742 MHz). The z displacements are anti-symmetric in y but are approximately constant in x . It can be seen in Figure 2.5 (a) and (b) that Surface 2 displaces in a bending motion about its weaker axis (x -axis) and Surface 1 rotates about the x -axis. The latter case of Surface 2 bending about the y -axis occurs in the second mode of the EZ subset (0.6914 MHz) with the expected displacement pattern shown in Figure 2.5 (c) and (d). The z displacements on Surface 2 vary in anti-symmetric fashion in the \hat{x} direction, but are approximately constant in the \hat{y} direction and Surface 3 rotates about the y -axis. Bending about the weaker axis corresponds to a more flexible orientation of the solid and therefore corresponds to a lower frequency of vibration. For the example discussed here, it is why the displacement pattern for the first EZ mode (bending about the weaker x -axis) has a lower frequency than the displacement pattern for the second EZ mode (bending about the stronger y -axis).

Other flexural modes occur in the EX subset (0.5899 MHz) and EY subset (0.8028 MHz). For the EX mode, it can be seen in Figure 2.3 (a) and (b) that Surface 3 bends about the z -axis and Surface 1 rotates about the z -axis. For the EY mode, it can be seen in Figure 2.4 (a) and (b) that Surface 1 bends about the z -axis and Surface 3 rotates about the z -axis.

Simple shear modes are characterized by a shearing motion and displacements predominantly located in one plane. The first and second OZ modes (0.6569 MHz and 1.2062 MHz, respectively) are shear modes involving predominantly ϵ_6 strain. This is characterized by displacement in the x - y plane. The second OX mode (0.8762 MHz) is also a shear mode and involves predominantly ϵ_4 strain, characterized by displacement in the y - z plane.

The MLCC can also deform in a manner in which displacements of the bounding surfaces are still normal to the surface, but have opposite signs over that surface. Modes with this displacement pattern occur in the OY subset (first mode=0.7011 MHz and second mode=0.9699 MHz). Figure 2.7 (b) and (d) shows that the original x - z bounding planes have displacements that are normal to the surface (i.e. in the \hat{y} direction) and vary in odd fashion about both the x and z -axes. This is made clear by observing that the originally horizontal centerlines in Figure 2.7 (b) and (d) remain horizontal. This deformation pattern is also present in the OX subset (first mode=0.7720 MHz and second mode=0.8762 MHz) where the originally vertical centerlines in Figure 2.6 (b) and (d) remain vertical. Overall, the y - z plane at the center of the capacitor remains unchanged for modes in the OX subset and the x - z plane at the center of the capacitor remains unchanged for modes in the OY subset.

One subset where results have not yet been discussed is the EV subset, which corresponds to primarily torsional displacements. The lowest mode and first natural frequency for this solid occurs in the EV subset (0.3543 MHz) and Figure 2.9 (a) and (b) shows twisting about the y -axis. The second EV mode (0.8621 MHz) is characterized by twisting about the z -axis and is shown in Figure 2.9 (c) and (d).

The last subset to discuss is the OD subset, which corresponds to primarily longitudinal vibration. The OD subset has displacements that do not change the initial symmetry of the object. As can be seen from Figure 2(a)–(c), the lowest mode shape (0.7088 MHz) involves primarily extension along the y -axis and is slightly concave (displacement inwards) on Surfaces 2 and 3 and convex (displacement outwards) on Surface 1. The displacements are reversed in the part of the vibrational cycle that is out of phase with that shown. At each point in the cycle, the sign of the displacements of the surface with the smallest area (Surface 1) is opposite to that of the two other surfaces, which is typical given the Poisson effect for this deformation pattern. The undistorted capacitor is shown in Figure 2.1 (b), (e), and (h) for clarification of differences between the modes. The second OD mode (0.8484 MHz) is shown in Figure 2.1 (d), (e), and (f) and is a higher-order version of the first OD mode, with a substantial component of the displacements along the y -axis, but phase variation along the x -axis. The third OD mode (0.9769 MHz) involves primarily extension/contraction along the x -axis (Figure 2.1 (g), (h), and (i)).

A comparison with the experimental frequency obtained for the third OD mode is discussed here, because it is the dominant mode excited through direct ferroelectric transduction [10]. The symmetry of the ferroelectric excitation has OD symmetry and a frequency of $0.99 \text{ MHz} \pm 0.01 \text{ MHz}$ was obtained, with a standard deviation previously published [10] for the measured set of these capacitors. This results in a 1.32% difference from the finite element calculations of 0.9769 MHz. The excitation symmetry has been described in previous work [32]. Future work from the authors will involve a comparison with the full experimental spectra.

4. CONCLUSIONS

Frequencies and associated vibrational modes of multilayer ceramic capacitors (MLCCs) were investigated by finite-element (FE) calculations. The first three frequencies and two displacement plots were presented for the MLCCs. As previously noted, OD modes are of great importance for comparison to experimental results, because the third mode in this subset is the dominant mode excited through direct ferroelectric transduction [10]; therefore the third mode shape for this subset was presented.

Conclusions of this study:

- Removal of the endcaps in the FE mesh,— done to reduce computation time while refining the mesh of the core region—increased the lowest frequency mode of each symmetry classification by an average of 3.4%, which is consistent with the subtraction of material. This result indicates that resonant frequencies of physical MLCCs are not greatly affected by variations in endcap geometry.
- The flexural mode shapes follow a pattern of bending characterized by displacements on bounding surfaces that act in a direction normal to the surface, vary in odd powers in one of the directions of the surface, and are approximately constant in the other direction. The lowest flexural mode is in the EZ subset (0.4742 MHz), which corresponds to bending motion of Surface 2 about the weaker axis (x -axis) and rotation of Surface 1 about the x -axis.
- Modes with predominantly shear displacements occur in the OZ and OX subsets.
- The lowest frequency overall is 0.3543 MHz is in the EV subset. It is characterized by primarily torsional displacements.
- The frequencies presented range from 0.3543 MHz to 0.8028 MHz for the first frequency in each subset, 0.6914 MHz to 1.2062 MHz for the second frequency in each subset, and 0.9769 MHz to 1.4184 MHz for the third frequency in each subset.
- For all subsets, the average percent increase from first to second mode for the MLCC is 56.7%. The average percent increase from second to third mode is 29.8%.
- There is a 1.32% difference between the finite element calculations and the ferroelectric excitation experimental findings for the frequency of the third OD mode.

These calculations of frequencies and mode shapes, which include all modal symmetries, will aid in interpreting RUS and resonant nonlinear ultrasonics measurements by enabling identification of measured vibrational modes. They also provide a basis for exploring dependence of resonant frequencies and nonlinear parameters on the location, size, and orientation of cracks. Therefore, the approach and results presented here are anticipated to serve a critical role in the development of nondestructive methods for detecting cracks in MLCCs and, thus, facilitating enhancements in the reliability of devices incorporating these capacitors.

REFERENCES

- [1] A. Teverovsky, Effect of manual-soldering-induced stresses on ceramic capacitors (part I). NASA Electronic Parts and Packaging (NEPP) Program, 2008.
- [2] D.S. Erdahl, I.C. Ume, Online-offline laser ultrasonic quality inspection tool for multilayer ceramic capacitors—Part I, *IEEE Trans. Adv. Packag.* 27 (2004) 647-653.
- [3] D.S. Erdahl, I.C. Ume, Online-offline laser ultrasonic quality inspection tool for multilayer ceramic capacitors—Part II, *IEEE Trans. Adv. Packag.* 28 (2005) 264-272.
- [4] O. Boser, P. Kellawon, R. Geyer, Electromechanical resonances in ceramic capacitors and their use for rapid nondestructive testing, *J. Am. Ceram. Soc.* 72 (1989) 2282-2286.
- [5] J. Pritchard, C.R. Bowen, F. Lowrie, Multilayer actuators: review, *Br. Ceram. Trans.* 100 (2001) 265-273.
- [6] K. Prume, R. Waser, K. Franken, H.R. Maier, Finite-element analysis of ceramic multilayer capacitors: modeling and electrical impedance spectroscopy for a nondestructive failure test, *J. Am. Ceram. Soc.* 83 (2000) 1153-1159.
- [7] A.D. Kostic, S.W. Schwartz, Optimized acoustic microscopy screening for multilayer ceramic capacitors, in: *Proceedings of the IEEE Reliability and Maintainability Symposium*, 2011, pp. 1-4.
- [8] S.A. Kim, W.L. Johnson, G.S. White, R. Roberts, Ultrasonic detection of defects in multilayered ceramic capacitors, in: *Proceedings of Materials and Processes for Medical Devices*, August 8-10, 2011, Minneapolis.
- [9] W.L. Johnson, S.A. Kim, T.P. Quinn, G.S. White, Nonlinear acoustic effects in multilayer ceramic capacitors, in: *Rev. Prog. Q. (AIP Conference Proceedings)*, vol. 1511, vols. 32A and 32B, 2013, pp. 1462-1469.
- [10] W.L. Johnson, S.A. Kim, G.S. White, J. Herzberger, in: *Proceedings of the 2014 IEEE International Ultrasonics Symposium*, 2014, pp. 244-247.
- [11] N.W. Ashcroft, N.D. Mermin, *Solid State Physics*, Holt, Rinehart, and Winston, New York (1976), p. 122.
- [12] G.S. White, C. Nguyen, B. Rawal, Young's modulus and thermal diffusivity measurements on barium titanate based dielectric ceramics, in: *Proceedings of Nondestructive Testing of High Performance Ceramics*, American Ceramic Society, Westerville, OH, 1987, pp. 371-379.
- [13] S.A. Kim, Off-diagonal orthorhombic-symmetry elastic constants, *Appl. Phys. Lett.* 65 (1994) 2949-2950.

- [14] H.M. Ledbetter, Orthotropic elastic stiffnesses of a boron–aluminum composite, *J. Appl. Phys.* 50 (1979) 8247–8248.
- [15] H.M. Ledbetter, J.F. LaBrecque, J.L. Dahnke, Propagation errors in elastic-constant inversion, *Phys. Status Solidi (A)* 67 (1981) 643–647.
- [16] M. Zgonik, P. Bernasconi, M. Duelli, R. Schlessler, P. Gunter, M.H. Garrett, D. Rytz, Y. Zhu, X. Wu, Dielectric, elastic, piezoelectric, electro-optic, and elasto-optic tensors of BaTiO₃ crystals, *Phys. Rev. B* 50 (1994) 5941–5949.
- [17] D. Berlincourt, H. Jaffe, Elastic and piezoelectric coefficients of single-crystal barium titanate, *Phys. Rev.* 111 (1958) 143–148.
- [18] H.M. Ledbetter, Monocrystal-polycrystal elastic-constant models, in: *Handbook of Elastic Properties of Solids, Liquids, and Gases*, vol. III, Academic Press, San Diego, 2001, pp. 313–324.
- [19] S. Urek, M. Drofenik, The hydrothermal synthesis of BaTiO₃ fine particles from hydroxide-alkoxide precursors, *J. Eur. Ceram. Soc.* 18 (1998) 279–286.
- [20] Y. Hiki, A.V. Granato, Anharmonicity in noble metals; higher order elastic constants, *Phys. Rev.* 144 (1966) 411.
- [21] S.G. Epstein, O.H. Carlson, The elastic constants of nickel-copper alloy single crystals, *Acta Metall.* 13 (1965) 487.
- [22] G. Simmons, H. Wang, *Single Crystal Elastic Constants and Calculated Aggregate Properties: A Handbook*, MIT Press, Cambridge, MA, 1971.
- [23] J.A. Rayne, B.S. Chandrasekhar, Elastic constants of β tin from 4.2 °K to 300 °K, *Phys. Rev.* 120 (1960) 1658–1663.
- [24] J.N. Reddy, *An Introduction to the Finite Element Method*, 3rd edition, McGraw-Hill, New York, NY, 2005.
- [25] R. Holland, Resonant properties of piezoelectric ceramic rectangular parallelepipeds, *J. Acoust. Soc. Am.* 43 (1968) 988–997.
- [26] M.W. Hyer, *Stress Analysis of Fiber-Reinforced Composite Materials*, McGraw-Hill, New York, NY, 1997.
- [27] B.A. Auld, *Acoustic Fields and Waves in Solids*, vol. I, Krieger, Malabar, FL, 1990.
- [28] O. Zienkiewicz, R. Taylor, J.Z. Zhu, *The Finite Element Method: Its Basis and Fundamentals*, 6th edition, Elsevier, Butterworth-Heinemann, Burlington, VT, 2005.

- [29] I. Ohno, Free vibration of a rectangular parallelepiped crystal and its application to determination of elastic constants of orthorhombic crystals, *J. Phys. Earth* 24 (1976) 355–379.
- [30] G.H. Golub, C.F. Van Loan, *Matrix Computations*, 4th ed., Johns-Hopkins University Press, Baltimore, MD, 2012.
- [31] J.F. Cornwell, *Group Theory in Physics*, vol. I, Academic Press, New York, 1984, Chapter 2.
- [32] W.L. Johnson, S.A. Kim, G.S. White, J. Herzberger, K.L. Peterson, P.R. Heyliger,
- [33] Time-domain analysis of resonant acoustic nonlinearity arising from cracks in multilayer ceramic capacitors, in: *AIP Conference Proceedings*, vol. 1706, 2016, p. 060005.

APPENDIX A: COEFFICIENT MATRICES

Elements of the coefficient matrices are given by

$$K_{ij}^{11} = \int_V \left(C_{11} \frac{\partial \phi_i^u}{\partial x} \frac{\partial \phi_j^u}{\partial x} + C_{55} \frac{\partial \phi_i^u}{\partial z} \frac{\partial \phi_j^u}{\partial z} + C_{66} \frac{\partial \phi_i^u}{\partial y} \frac{\partial \phi_j^u}{\partial y} \right) \partial V$$

$$K_{ij}^{12} = \int_V \left(C_{12} \frac{\partial \phi_i^u}{\partial x} \frac{\partial \phi_j^v}{\partial y} + C_{66} \frac{\partial \phi_i^u}{\partial y} \frac{\partial \phi_j^v}{\partial x} \right) \partial V = K_{ji}^{21}$$

$$K_{ij}^{13} = \int_V \left(C_{13} \frac{\partial \phi_i^u}{\partial x} \frac{\partial \phi_j^w}{\partial z} + C_{55} \frac{\partial \phi_i^u}{\partial z} \frac{\partial \phi_j^w}{\partial x} \right) \partial V = K_{ji}^{31}$$

$$K_{ij}^{22} = \int_V \left(C_{22} \frac{\partial \phi_i^v}{\partial y} \frac{\partial \phi_j^v}{\partial y} + C_{44} \frac{\partial \phi_i^v}{\partial z} \frac{\partial \phi_j^v}{\partial z} + C_{66} \frac{\partial \phi_i^v}{\partial x} \frac{\partial \phi_j^v}{\partial x} \right) \partial V$$

$$K_{ij}^{23} = \int_V \left(C_{23} \frac{\partial \phi_i^v}{\partial y} \frac{\partial \phi_j^w}{\partial z} + C_{44} \frac{\partial \phi_i^v}{\partial z} \frac{\partial \phi_j^w}{\partial y} \right) \partial V$$

$$K_{ij}^{33} = \int_V \left(C_{33} \frac{\partial \phi_i^w}{\partial z} \frac{\partial \phi_j^w}{\partial z} + C_{44} \frac{\partial \phi_i^w}{\partial y} \frac{\partial \phi_j^w}{\partial y} + C_{55} \frac{\partial \phi_i^w}{\partial x} \frac{\partial \phi_j^w}{\partial x} \right) \partial V$$

Elements of the mass matrices are given by

$$M_{ij}^{11} = \int_V (\rho \psi_i^u \psi_j^u) dV$$

$$M_{ij}^{22} = \int_V (\rho \psi_i^v \psi_j^v) dV$$

$$M_{ij}^{33} = \int_V (\rho \psi_i^w \psi_j^w) dV$$